Article:
Chi, Y, Xu, L and Yu, H-S (2014) Constitutive modeling of steel-polypropylene hybrid fiber reinforced concrete using a non-associated plasticity and its numerical implementation. Composite Structures, 111. pp. 497-509. ISSN 0263-8223

https://doi.org/10.1016/j.compstruct.2014.01.025

Constitutive Modeling of Steel-Polypropylene Hybrid Fiber Reinforced Concrete with a Non-associated Plasticity and Its Numerical Implementation

Yin Chi[a], Lihua Xu[b,*], Hai-sui Yu[a]

[a]*Faculty of Engineering, The University of Nottingham, Coates Building, University Park, Nottingham, NG72RD, United Kingdom*

[b] *School of Civil Engineering, Wuhan University, 8 Dong Hu South Road, WuChang district, 430072, China*

Abstract: This paper firstly presents a non-associated plasticity-based constitutive model for hybrid steel-polypropylene fiber reinforced concrete (HFRC) materials in an attempt to characterize the stress-strain responses under multiaxial loading scenarios. Together with a five-parameter loading surface and uncoupled hardening and softening regimes, a nonlinear plastic potential function is particularly introduced into the constitutive model with the material constants experimentally determined, which allows a more accurate estimation of the volumetric dilatency of HFRC. Moreover, the influence of fiber parameters on the plastic flow direction is also addressed. The developed model is then implemented into ABAQUS finite element package through a user-defined material (UMAT) subroutine that can be applicable for the convenient use in numerical simulation of HFRC materials. A substepping scheme with error control for integrating elasto-plastic stress-strain rate equations is presented in detail. Subsequently, the proposed model is evaluated by available multiaxial compression test results of both plain concrete and FRC reported by other researchers. It is shown that the constitutive model can realistically capture the stress-strain responses as well as the volumetric deformation of HFRC having various fiber reinforcement indices.

Keywords: Non-associated plasticity; Fiber reinforced concrete; Constitutive model; Multiaxial

*Corresponding author, Lihua Xu, Professor, School of Civil Engineering, Wuhan University, xulihua-d@126.com, 8 Dong Hu South Road, Wuhan University(North gate), WuChang district, 430072. Tel: +86(0)27 68775337. Fax: +86 (0)27 68775328

compression; Implementation; ABAQUS;

1 Introduction

Over the past few decades, considerable research efforts have been invested in the development of elasto-plastic constitutive models for plain concrete (Imran and Pantazopoulou, 2001; Grassl et al., 2002; Park and Kim, 2005; Papanikolaou and Kappos, 2007). Some of such models have been successfully incorporated into commercial finite element codes and extensively utilized for the numerical simulation of concrete structures. The achievements allow researchers to investigate the mechanical behavior of plain concrete conveniently by selecting the corresponding constitutive models.

With the rapid development of fiber reinforced concrete (FRC) theory and its applications, FRC materials such as steel fiber reinforced concrete, polypropylene fiber reinforced concrete, or hybrid steel-polypropylene fiber reinforced concrete have gained wide recognition and have become firmly established within the arsenal of existing construction materials over recent years. FRC exhibits excellent tensile, bending and shearing strength as well as superb resistance to cracking, impact and fatigue. The substantial amount of research and development in fiber reinforcing technology has led to a wide range of practical engineering applications such as in pavement design, structural repair/maintenance, shot concrete mix design, deep beams and in offshore environments (offshore foundation, condeep platform floats, support structures and storage unit for nature oil or gas), etc. (ACI Committee 544., 1982; Swamy and Barr, 1989; Bentur and Mindess, 1990). Nowadays, owing to the rapid improvements in numerical simulation techniques and computational capabilities, engineers have begun to simulate the behavior of FRC structures in addition to traditional concrete structures using finite element modeling (FEM) to

analyze and solve various concrete problems as subjected to complicated loading conditions. The analysis of an engineering problem using FEM essentially involves solving equilibrium equations with prescribed boundary and initial conditions that are linked by the material's constitutive relations (Babu et al., 2005), in which the constitutive model plays a significant role in the numerical simulation. It is a fact that many attempts concerning on constitutive modeling of FRC materials with steel fiber reinforced concrete (SFRC) in particular have achieved certain success (e.g. Chern et al., 1992; Murugappan et al., 1993; Song et al., 1996; Hu et al., 2003; Seow and Swaddiwudhipong, 2005; Lu and Hsu, 2006). It is acknowledged that FRC materials exhibit complex responses in terms of strain hardening/softening, volumetric dilatency, pressure sensitivity, etc., which change significantly with the varying fiber parameters. However, to the authors' knowledge, the majority of the published models depend to a large degree on their particular application, and with respect to HFRC materials, a unified constitutive model along with the incorporation into FE software package can barely be found in the literature. As HFRC materials are typically subjected to multiaxial loadings, a more sophisticated constitutive model is imperatively required for the accurate prediction of the stress state and the deformation.

To this end, the subsequent focus of this study is to develop a constitutive model for HFRC material predicated on a non-associated plasticity which is a continuation of research (Chi et al., 2013). Furthermore, the proposed constitutive model is implemented into FE software package ABAQUS by an explicit integration method using the UMAT subroutine. Finally, the response of the developed model is validated and verified with existing experimental results in terms of stress-strain behavior and volumetric deformation under various loadings.

2 Constitutive modeling

2.1 Loading surface of HFRC

The mathematical form of the loading surface proposed in present study is developed on the basis of the Willam-Warnke (1974) (W-W) five-parameter failure model, which is expressed using the Haigh-Westergaard coordinates as shown below:

$$f(\xi,\rho,\theta)=\sqrt{2J_2}-K(\bar{\varepsilon}_p)\cdot\rho^{hf}(\xi,\theta)=0 \tag{1}$$

where $K(\bar{\varepsilon}_p)$ is the hardening/softening function that defines the increase of strength during hardening and the strength deterioration during softening, which is governed by the equivalent plastic strain, ranging from K_0 to 1. The function $\rho^{hf}(\xi,\theta)$ defines the parabolic shape of meridians which binds the ultimate strength of HFRC (Eq.4). It is interpolated between the tensile meridian ρ_t (Eq.2) where Lode angle θ=0°, and the compressive meridian ρ_c (Eq.3) where Lode angle $\theta=60°$ as follows:

$$\frac{\xi}{f_{cu}}=a_2\left(\frac{k_t\rho_t}{f_{cu}}\right)^2+a_1\left(\frac{k_t\rho_t}{f_{cu}}\right)+a_0 \tag{2}$$

$$\frac{\xi}{f_{cu}}=b_2\left(\frac{k_c\rho_c}{f_{cu}}\right)^2+b_1\left(\frac{k_c\rho_c}{f_{cu}}\right)+b_0 \tag{3}$$

$$\begin{aligned}\rho^{hf}(\xi,\theta)=&\frac{2\rho_c^{hf}[(\rho_c^{hf})^2-(\rho_t^{hf})^2\cos\theta]}{4[(\rho_c^{hf})^2-(\rho_t^{hf})^2]\cos^2\theta+(\rho_c^{hf}-2\rho_t^{hf})^2}\\&+\frac{\rho_c^{hf}(2\rho_t^{hf}-\rho_c^{hf})\{4[(\rho_c^{hf})^2-(\rho_t^{hf})^2]\cos^2\theta+5(\rho_t^{hf})^2-4\rho_t^{hf}\rho_c^{hf}\}^{1/2}}{4[(\rho_c^{hf})^2-(\rho_t^{hf})^2]\cos^2\theta+(\rho_c^{hf}-2\rho_t^{hf})^2}\end{aligned} \tag{4}$$

where $\rho_t^{hf}=k_t\rho_t,\rho_c^{hf}=k_c\rho_c$ and $\cos\theta=\dfrac{2\sigma_3-\sigma_2-\sigma_1}{2\sqrt{3}\sqrt{J_2}}$ for $\sigma_3\geq\sigma_2\geq\sigma_1$. The interpolated meridian function $\rho^{hf}(\xi,\theta)$ forms a cone-shaped failure envelope, as schematically illustrated in Fig.1. f_{cu} denotes the uniaxial compressive strength of plain concrete. The equations are expressed in terms of hydrostatic pressure ξ and deviatoric stress ρ, where $\xi=I_1/\sqrt{3}$ and $\rho=\sqrt{2J_2}$ ($I_1=tr(\sigma_i)/3$ is the first invariant of stress tensor,

and $J_2 = \frac{1}{2} s_{ij} s_{ij}$ is the second invariant of deviatoric stress tensor). $\sigma_i (i = 1,2,3)$ is the principal normal stress in the *i*th direction. The material constant $a_0, a_1, a_2, b_0, b_1, b_2$ are determined from a large variety of experimental data points, which relate to the uniaxial strength, uniaxial tensile strength, equal biaxial compressive strength and the triaxial strength with high confinement, the values are given in Chi et al 2013. Since the W-W model has shown its robustness in prediction of failure strengths of various concrete materials, and the model's failure envelope also satisfies the requirements of smoothness, convexity with separate descriptions of the compressive and tensile meridian, these features allows flexible modification of a specific section to account for the presence of hybrid fibers.

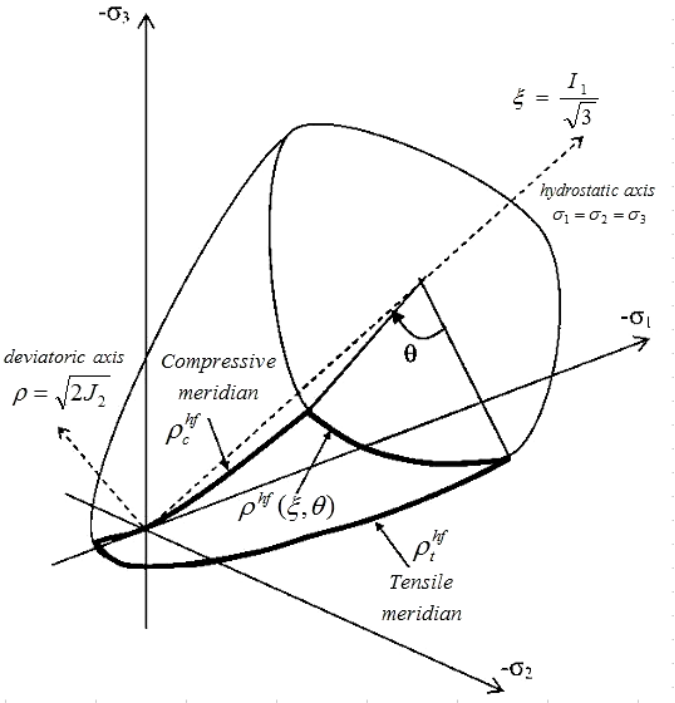

Fig.1 Schematic diagram of failure envelop in Haigh-Westergaard coordinates

Consequently, it is noted from Eq.2 to Eq.4 that, in this study, two coefficients (k_c, k_t) are introduced into the meridional functions to account for the increase in stress state at failure along both meridians, which will also result in a change in the entire failure envelop that can reflect the fiber effect subject to other loading scenarios. These two coefficients are calibrated based on true

triaxial compression tests as described in following section.

2.2 Experimental program

Cubic specimens were prepared for true triaxial compression testing using 18 HFRC mixes (Table 1), containing 0%, 0.5%, 1.0% and 1.5% volume fraction of corrugated steel fibers with aspect ratio of 30 and 60, and 0%, 0.05%, 0.1% and 0.15% volume fraction of monofilament polypropylene fibers with aspect ratio of 167 and 396. For comparison, plain concrete as well as single fiber reinforced concrete were also tested (Table 2). Ordinary Portland cement (P.O 42.5) was used as the binder for the matrix mixtures. The mix proportion of cement:water:sand:coarse aggregate by weight was in the ratio of 1:0.34:1.80:2.49. The steel fibers with the trade name *Hansen* have a minimum tensile strength of 600MPa and density of 7800kg/m^3. The polypropylene fibers with the trade name *CTA* have a minimum tensile strength of 400MPa and an elongation rate between 15-35%. Specimens of size 150×150×150mm were cast in cubic-shaped steel moulds and compacted on a vibration table. All the specimens were demolded after 24 hours and stored in a curing room at a temperature of 20±2^{o}C and a relative humidity of 95% until 28 days strength was achieved. The plain concrete matrix is specified with a 28-day compressive strength of 60MPa. All the specimens were then tested using a true triaxial testing set-up (see Fig.2) with lateral pressures ($\sigma_1 < \sigma_2$) designated at 5/10MPa, 4/15MPa and 3/20 MPa respectively. A displacement control with a 0.05mm/s loading velocity was applied in the axial direction (σ_3 direction) by actuators until ultimate failure occurred. All the specimens to be tested were covered in a plastic membrane and lubrication was applied between the contact interfaces of the specimen and rigid loading platens to eliminate the undesired end constraint induced by friction. All the pressures were measured by pressure transducers. Axial and lateral

extensometers were used to measure the deformations caused by the imposed stresses. The test results of all the specimens with respect to stresses and axial strains at failure under true triaxial compressions were summarized in Tables (3), (4) and (5), where the listed triaxial strength for each loading scenario was the average value from three test specimens.

Table 1. Variables of HFRC for the triaxial compression test

No.	Specimen Number	Volume fraction of SF/%	Volume fraction of PF /%	Aspect ratio of SF	Aspect ratio of PF	No.	Specimen Number	Volume fraction of SF/%	Volume fraction of PF /%	Aspect ratio of SF	Aspect ratio of PF
1	SA05PA05	0.5	0.05	30	167	10	SB10PA10	1.0	0.10	60	167
2	SA05PB05	0.5	0.05	30	396	11	SB10PB10	1.0	0.10	60	396
3	SB05PA05	0.5	0.05	60	167	12	SA10PA15	1.0	0.15	30	167
4	SB05PB05	0.5	0.05	60	396	13	SA15PA05	1.5	0.05	30	167
5	SA05PA10	0.5	0.10	30	167	14	SA15PA10	1.5	0.10	30	167
6	SA05PA15	0.5	0.15	30	167	15	SA15PA15	1.5	0.15	30	167
7	SA10PA05	1.0	0.05	30	167	16	SA15PB15	1.5	0.15	30	396
8	SA10PA10	1.0	0.10	30	167	17	SB15PA15	1.5	0.15	60	167
9	SA10PB10	1.0	0.10	30	396	18	SB15PB15	1.5	0.15	60	396

Table 2. Variables of single fiber reinforced concrete

No.	Specimen Number	Volume fraction of SF/%	Volume fraction of PF /%	Aspect ratio of SF	Aspect ratio of PF
19	SA05	0.5	-	30	-
20	SA10	1.0	-	30	-
21	SA15	1.5	-	30	-
22	PA05	-	0.05	-	167
23	PA10	-	0.10	-	167
24	PA15	-	0.15	-	167
25	C60	-	-	-	-

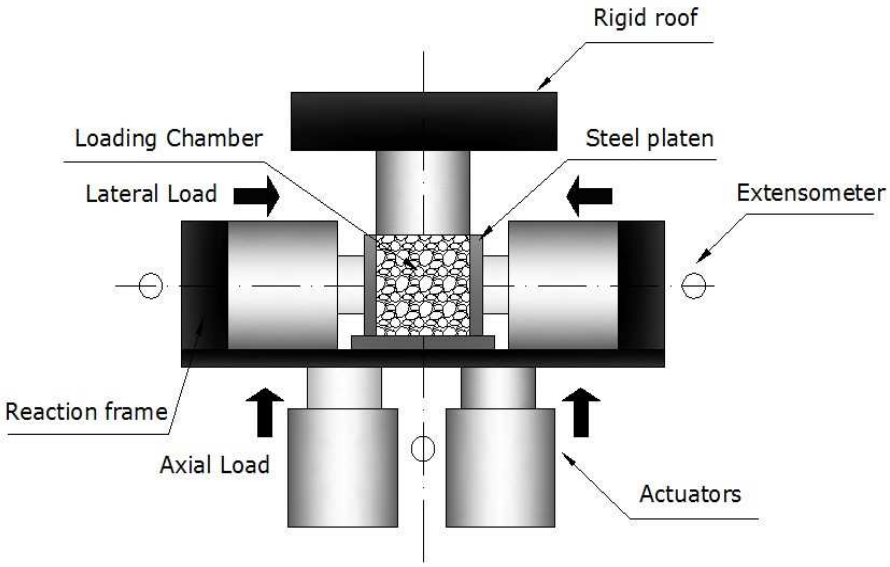

Fig.2 True triaxial compression testing set-up

Table 3. Peak stresses and strains at lateral pressure combination of 5/10MPa

No.	Specimen	$-\sigma_1$ (MPa)	$-\sigma_2$ (MPa)	$-\sigma_3$ (MPa)	ε_1	ε_2	ε_3	$tan\phi$
1	SA05PA05	5.02	9.95	106.63	-0.01201	0.00563	0.01681	3.83
2	SA05PB05	5.15	9.92	109.09	-0.01121	0.00491	0.01756	3.44
3	SB05PA05	5.05	9.93	115.20	-0.01627	0.00539	0.02261	4.60
4	SB05PB05	5.05	9.92	118.69	-0.01515	0.00382	0.02103	5.42
5	SA05PA10	5.11	9.87	107.18	-0.01491	0.00463	0.01585	10.17
6	SA05PA15	5.02	9.91	109.09	-0.01369	0.00694	0.01628	4.63
7	SA10PA05	5.10	9.98	111.29	-0.01235	0.00533	0.01591	4.67
8	SA10PA10	5.06	9.81	109.19	-0.01316	0.00458	0.01486	7.60
9	SA10PB10	5.09	9.91	109.67	-0.01411	0.00631	0.01319	9.96
10	SB10PA10	5.06	9.98	113.45	-0.01399	0.00511	0.01526	7.96
11	SB10PB10	5.10	9.92	115.19	-0.01745	0.00592	0.01631	15.82
12	SA10PA15	5.09	9.90	115.74	-0.00840	0.00109	0.01349	5.74
13	SA15PA05	5.03	9.85	115.25	-0.01271	0.00840	0.00873	13.32
14	SA15PA10	5.05	9.94	116.20	-0.01933	0.00670	0.01094	9.06
15	SA15PA15	5.08	9.83	115.73	-0.01970	0.00373	0.01197	5.72
16	SA15PB15	5.17	9.97	120.83	-0.01759	0.00383	0.01209	8.09
17	SB15PA15	4.99	9.84	119.37	-0.01880	0.00232	0.01422	7.79
18	SB15PB15	5.14	9.79	118.47	-0.01945	0.00223	0.01683	14.30
19	SA05	5.13	9.95	107.61	-0.01003	0.00295	0.01129	11.21
20	SA10	5.06	9.82	118.94	-0.01149	0.00230	0.01358	13.24
21	SA15	5.14	9.81	124.23	-0.01309	0.00105	0.01252	12.98
22	PA05	5.15	9.92	107.54	-0.01221	0.00308	0.02262	3.38
23	PA10	5.09	9.91	99.24	-0.01349	0.00230	0.02512	3.64
24	PA15	5.22	9.87	93.80	-0.01546	0.00151	0.02623	4.58
25	C60	4.94	9.88	85.02	-0.01250	0.00069	0.00998	6.71

Table 4 Peak stresses and strains at lateral pressure combination of 4/15MPa

No.	Specimen	$-\sigma_1$ (MPa)	$-\sigma_2$ (MPa)	$-\sigma_3$ (MPa)	ε_1	ε_2	ε_3	$tan\phi$
1	SA05PA05	3.85	15.58	110.76	-0.01715	0.00125	0.01266	5.82
2	SA05PB05	3.95	15.55	107.43	-0.00572	0.00042	0.01490	2.88
3	SB05PA05	3.94	15.44	125.28	-0.02443	0.00060	0.01226	2.91
4	SB05PB05	4.05	15.55	113.19	-0.00774	0.00079	0.01621	3.59
5	SA05PA10	3.92	15.65	109.52	-0.00801	0.00069	0.01666	3.67
6	SA05PA15	3.98	15.40	112.15	-0.00470	0.00080	0.01517	2.24
7	SA10PA05	3.68	15.57	113.27	-0.00339	0.00173	0.00929	2.04
8	SA10PA10	3.82	15.76	108.85	-0.00360	0.00110	0.01625	1.78
9	SA10PB10	3.97	15.58	102.53	-0.01525	0.00099	0.00967	3.99
10	SB10PA10	3.89	15.59	132.73	-0.01223	0.00526	0.01229	10.26
11	SB10PB10	3.88	15.43	116.52	-0.01095	0.00491	0.01379	4.97
12	SA10PA15	3.97	15.61	115.67	-0.00705	0.00192	0.02286	2.11
13	SA15PA05	3.86	15.29	122.39	-0.01105	0.00626	0.01645	3.23
14	SA15PA10	4.04	15.40	126.38	-0.01332	0.00344	0.01612	8.64
15	SA15PA15	3.86	15.41	118.88	-0.01404	0.00212	0.01655	15.27
16	SA15PB15	3.93	15.24	113.86	-0.01607	0.00248	0.00984	4.66
17	SB15PA15	3.78	15.33	124.90	-0.01209	0.00299	0.00938	9.73
18	SB15PB15	3.87	15.40	108.34	-0.01093	0.00297	0.00901	16.85
19	SA05	3.93	15.83	111.38	-0.00928	0.00034	0.00758	4.38
20	SA10	3.93	15.42	116.02	-0.01248	0.00155	0.00738	3.49
21	SA15	3.90	15.35	121.29	-0.01221	0.00114	0.00734	3.21
22	PA05	3.91	15.82	110.83	-0.01181	0.00308	0.00738	5.68
23	PA10	3.82	15.26	101.66	-0.01547	0.00570	0.00841	8.20
24	PA15	3.82	15.43	97.38	-0.01963	0.00174	0.01593	9.83
25	C60	3.74	15.53	86.75	-0.01109	0.00088	0.00795	4.85

Table 5 Peak stresses and strains at lateral pressure combination of 3/20MPa

No.	Specimen	$-\sigma_1$ (MPa)	$-\sigma_2$ (MPa)	$-\sigma_3$ (MPa)	ε_1	ε_2	ε_3	$tan\phi$
1	SA05PA05	3.12	19.89	115.52	-0.00413	0.00151	0.02243	1.67
2	SA05PB05	2.94	20.43	115.50	-0.00102	-0.00167	0.01715	1.75
3	SB05PA05	2.94	19.64	127.31	-0.00582	-0.00037	0.01535	3.26
4	SB05PB05	2.90	19.45	109.78	-0.00686	-0.00079	0.01455	4.87
5	SA05PA10	2.95	19.70	112.35	-0.00791	-0.00027	0.01613	4.53
6	SA05PA15	2.92	20.04	120.84	-0.00487	0.00056	0.01145	3.27
7	SA10PA05	2.92	19.55	118.07	-0.00175	-0.00175	0.01912	1.84
8	SA10PA10	2.99	20.16	118.12	-0.00167	-0.00026	0.00728	2.24
9	SA10PB10	2.96	19.93	112.88	-0.00867	0.00007	0.02251	2.99
10	SB10PA10	2.81	19.94	106.17	-0.01103	0.00003	0.02095	4.59
11	SB10PB10	2.91	20.06	133.95	-0.01088	0.00050	0.01943	5.06
12	SA10PA15	3.01	19.96	128.48	-0.00336	-0.00003	0.01155	2.43
13	SA15PA05	2.90	19.89	121.83	-0.00572	0.00061	0.01021	5.73
14	SA15PA10	3.01	20.28	129.12	-0.00989	-0.00030	0.00969	5.69
15	SA15PA15	2.83	19.98	134.00	-0.00788	-0.00030	0.00840	5.43
16	SA15PB15	2.85	19.86	123.29	-0.00542	-0.00033	0.01523	3.01
17	SB15PA15	3.02	19.74	133.43	-0.00642	-0.00027	0.01359	4.65
18	SB15PB15	3.04	19.81	125.38	-0.00741	-0.00025	0.01476	4.96
19	SA05	3.03	20.43	114.66	-0.00380	-0.00080	0.01415	2.58
20	SA10	2.97	20.17	119.72	-0.00350	-0.00084	0.01052	3.52
21	SA15	2.98	20.00	130.65	-0.00465	-0.00059	0.00983	6.76
22	PA05	3.00	20.10	114.94	-0.00293	-0.00080	0.02263	1.79
23	PA10	2.94	20.30	111.66	-0.00230	-0.00070	0.01483	1.92
24	PA15	3.11	19.85	112.92	-0.00351	-0.00067	0.01939	1.99
25	C60	3.16	20.34	86.45	-0.00429	-0.00060	0.01274	3.08

The values of k_c, k_t were then respectively accessed and calibrated to the following equations according to the uniaxial compression test results of the literature (Zhang, 2010) and the true triaxial compression test results in present study (Tables (3), (4) and (5)), relating to the volume fraction and aspect ratio of both steel and polypropylene fiber, given by Eqs.(5) and (6), the detailed calibration approach was reported in literature (Chi et al, 2013):

$$k_c = 1 + 0.056\lambda_{sf} \tag{5}$$

$$k_t = 1 + 0.08\lambda_{sf} + 0.132\lambda_{pf} \tag{6}$$

where λ_{sf} denotes the fiber reinforcement index (FRI) of steel fiber calculated as $\lambda_{sf} = V_{sf}\frac{l_{sf}}{d_{sf}}$ (V_{sf} is the volume fraction of steel fiber and $\frac{l_{sf}}{d_{sf}}$ is the aspect ratio of steel fiber). λ_{pf} denotes the FRI of polypropylene fiber calculated as $\lambda_{pf} = V_{pf}\frac{l_{pf}}{d_{pf}}$ (V_{pf} is the volume fraction of polypropylene fiber and $\frac{l_{pf}}{d_{pf}}$ is the aspect ratio of polypropylene fiber).

It can be inferred from Eqs.(5) and (6) that as the FRI of steel fiber increases, both the predicted compressive and tensile meridians are expanded. However, the FRI of polypropylene fiber has shown certain improvement for the tensile meridian rather than compressive meridian. This observation concurs with many other experimental evidences (Bayasi and Zeng,1993; Tavakoli, 1994; Qian and Stroeven, 2000; Xu et al, 2007), that polypropylene fiber has insignificant impact on the uniaxial compressive strength, of which the stress state is lying on the compressive meridian (Lode angle $\theta = 60^{\circ}$). Fig.3 shows the variation of failure envelope with the change of k_c and k_t values in π plane. As can be seen that, the deviatoric tracings approach the triangular shape as the k_c value increases, and the shape gradually becomes circular for increasing k_t values.

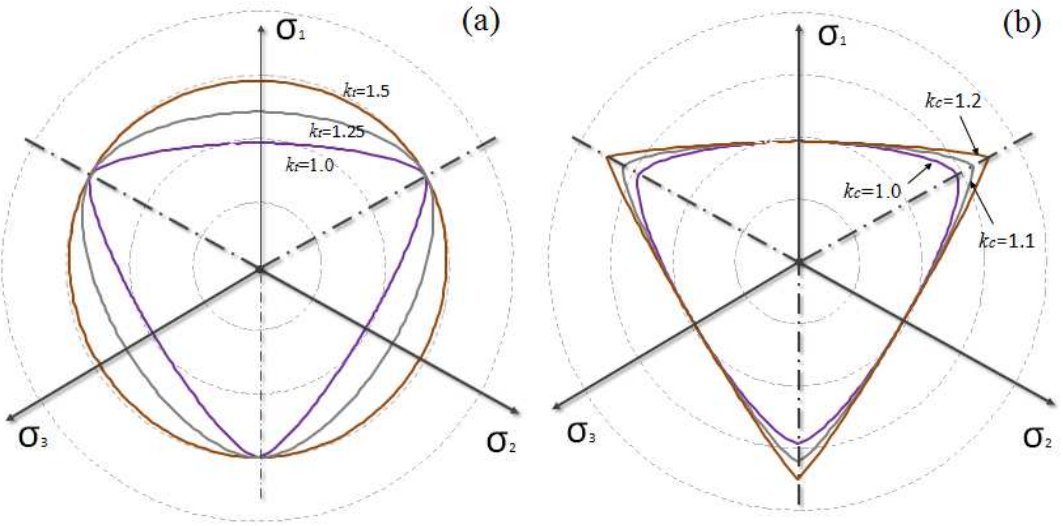

Fig.3 Variation of failure envelope with the change of k_t (a) and k_c (b) values

2.3 Hardening and softening law

The hardening/softening rule define the shape and location of the loading surface as well as the material's response after initial yielding, wherein the hardening describes the pre-peak behavior as the elastic region terminates and softening corresponds to the post-peak behavior during plastic flow. In the present formulation, the HFRC is assumed to remain isotropic during the whole loading process. The loading surfaces can be explicitly generated corresponding to the individual hardening/softening parameter $\bar{\varepsilon}_p$ (i.e the equivalent plastic strain). The mathematical description of the hardening and softening function were derived from Guo (1997) parabola. For its numerical implementation, they were generalized and differentiated as a rate form, given by:

For hardening regime, $\bar{\varepsilon} \le \varepsilon_c$:

$$dK(\bar{\varepsilon}_p) = \left[a\frac{1}{\varepsilon_c} + 2(3-2a)\left(\frac{\bar{\varepsilon}}{\varepsilon_c}\right)\frac{1}{\varepsilon_c} + 3(a-2)\left(\frac{\bar{\varepsilon}}{\varepsilon_c}\right)^2\frac{1}{\varepsilon_c} \right] \cdot d\bar{\varepsilon}_p = H_p(k,s)\cdot d\bar{\varepsilon}_p \qquad (7)$$

For softening regime, $\bar{\varepsilon} \ge \varepsilon_c$:

$$dK(\bar{\varepsilon}_p)=\frac{\frac{1}{\varepsilon_c}\left[b\left(\frac{\bar{\varepsilon}}{\varepsilon_c}-1\right)^2+\frac{\bar{\varepsilon}}{\varepsilon_c}\right]-\frac{\bar{\varepsilon}}{\varepsilon_c}\left[2b\left(\frac{\bar{\varepsilon}}{\varepsilon_c}-1\right)\frac{1}{\varepsilon_c}+\frac{1}{\varepsilon_c}\right]}{\left[b\left(\frac{\bar{\varepsilon}}{\varepsilon_c}-1\right)^2+\frac{\bar{\varepsilon}}{\varepsilon_c}\right]^2}\cdot d\bar{\varepsilon}_p=H_p(k,s)\cdot d\bar{\varepsilon}_p \tag{8}$$

where $H_p(k,s)$ is the hardening/softening modulus, and $\bar{\varepsilon}$ denotes the total equivalent strain at current increment step, calculated with respect to three-dimensional stress state (Yu, 2006):

$$\bar{\varepsilon}=\frac{1}{3}\left\{2\left[\left(\varepsilon_{xx}-\varepsilon_{yy}\right)^2+\left(\varepsilon_{yy}-\varepsilon_{zz}\right)^2+\left(\varepsilon_{xx}-\varepsilon_{zz}\right)^2\right]+3\left(\varepsilon_{xy}^2+\varepsilon_{yz}^2+\varepsilon_{zx}^2\right)\right\}^{\frac{1}{2}} \tag{9}$$

It is noted in Eq.(7) that the coefficient a is a parameter related to the FRI of hybrid fibers which controls the slope of hardening curve to enable the hardening rule to account for the presence of hybrid fibers. It was determined according to literature (Zhang, 2010) through a uniaxial compression test, and regressed as:

$$a=28.2283-23.2771 f_{fc}{}^{0.0374}+0.4772\lambda_{sf}-0.4917\lambda_{pf} \tag{10}$$

In addition, the notation ε_c represents the amount of equivalent strain when the stress state reaches the failure surface. Once the equivalent strain $\bar{\varepsilon}$ in current increment step is calculated to be equal to the specified ε_c (i.e $\bar{\varepsilon}=\varepsilon_c$), resulting a zero hardening modulus, which means that the stress state has reached to the peak and the softening will take place. Here, for derivation of the ε_c of HFRC under multiaxial stresses, a linear relationship between a confinement level ($(\sigma_1+\sigma_2)/f_c$) and the strain amplification ($\varepsilon_c/\varepsilon_q$) is developed based on the true triaxial test results according to reference (Papanikolaou and Kappos, 2007), where ε_q the corresponding equivalent strain of HFRC at its uniaxial compressive strength is calculated as:

$$\varepsilon_q=\frac{2}{3}\left(\varepsilon_3-\varepsilon_1\right) \tag{11}$$

The recommended value of ε_q is given by:

$$\varepsilon_q = 263.3\sqrt{f_{cu}(1+0.206\lambda_{sf}+0.388\lambda_{pf})}\times 10^{-6} \tag{12}$$

and the predictive equation for ε_c relating to the confinement level is then developed based on the true triaxial test results shown as the following equation:

$$\varepsilon_c = \varepsilon_q \cdot \left(1 + 20 \cdot \frac{\sigma_1 + \sigma_2}{f_{cu}}\right) \tag{13}$$

where σ_1, σ_2 represent the applied lateral pressure respectively, which reduces to $\varepsilon_c = \varepsilon_q$ when subjected to uniaxial compression.

Moreover, the coefficient b in Eq.(8) is also a parameter relating to the FRI of hybrid fibers, which controls the slope of the softening function that can be calibrated with the true triaxial experimental results to enable the softening rule to simulate the varying softening behavior as the fiber reinforcement index changes. The b value was developed and computed using the following equation:

$$b = 0.01 + 0.037 f_{fc}^{\ 0.2846} - 0.02372\lambda_{sf} - 0.2335\lambda_{pf} \tag{14}$$

Consequently, at the end of each finite time interval $t_{n+1} = t_n + \Delta t$, the value of hardening/softening function is updated as:

$$K_{n+1} = K_n + dK_n(\bar{\varepsilon}_p) \tag{15}$$

Fig.4 shows the evolution of the compressive and tensile meridians for different values of hardening/softening function during the plastic flow, and Fig.5 illustrates the evolution of both the hardening and softening regimes with respect to changing *a* and *b* values. It is worth noting that the proposed model is able to describe the various stress-strain behaviors that are usually arise as a result of varying fiber content.

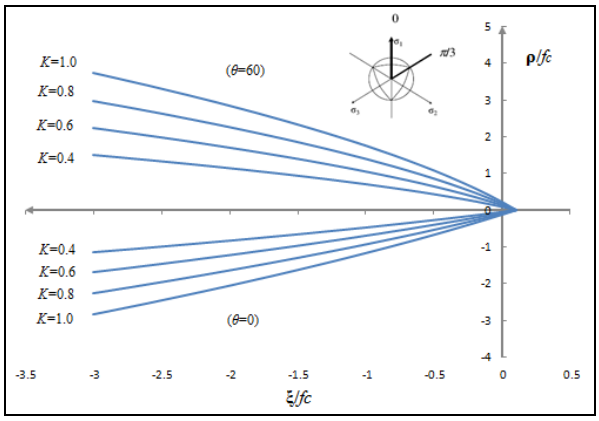

Fig.4 Evolution of meridians

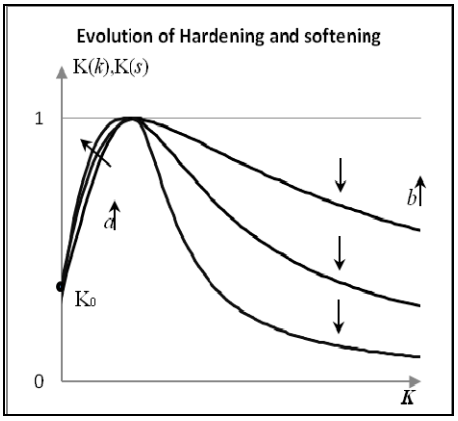

Fig.5 Evolution of hardening and softening

2.4 Non-associated flow rule

After ascribing a failure criterion and hardening/softening law to the initial and the subsequent surfaces, it remains to determine the plastic strain once the current yield surface is reached. According to the theory of plasticity, the loading surface function and the stress-strain relation are connected by a plastic flow rule which defines both the magnitude and direction of the plastic strain increment, the evolution of the plastic strain rate is expressed by:

$$d\varepsilon_{ij}^{p} = d\lambda \frac{\partial g}{\partial \sigma_{ij}} \tag{16}$$

In present study, we assumed a non-associated plastic flow for HFRC materials, namely, $g \neq f$. The plastic potential function has the following expression in Haigh-Westergaard stress space, which was developed based on Grassal et al.(2002) model for plain concrete, given by:

$$g = \xi + \alpha\rho + \beta\rho^{2} + const = 0 \tag{17}$$

where the coefficients α, β are material constants calibrated according to the true triaxial compression test results in terms of peak stresses and peak strains. It has to be noted that, for a more convenient calibration of these two coefficients, we also assumed that the plastic flow of HFRC is Lode angle independent, meaning that the plastic flow directions are all identical on a deviatoric plane within the same hydrostatic stress (See Fig.6). In addition, another basic

hypothesis is that the inclination of the total plastic strain is always equal to the inclination of the plastic strain increment, as indicated in Fig.7. Consequently, the inclination can be calculated by the derivation of plastic potential function (Imran and Pantazopoulou, 2001):

$$\phi = \tan\phi = \frac{\rho'}{\xi'} = -\frac{d\xi}{d\rho} \tag{18}$$

After substituting Eq.(18) into Eq.(17), we get:

$$\phi = -\frac{d\xi}{d\rho} = \alpha + 2\beta\rho \tag{19}$$

Based on the true triaxial test results，the coefficients α, β were then calibrated through two kinds of loading combinations. Here, we specify ϕ_1, ρ_1 and ϕ_2, ρ_2 respectively correspond to the plastic inclination and deviatoric stress of the selected two boundary conditions, written as:

$$\phi_1 = \alpha + 2\beta\rho_1 \tag{20}$$

$$\phi_2 = \alpha + 2\beta\rho_2 \tag{21}$$

by solving the above equation, coefficients α, β can be obtained as follows:

$$\alpha = \phi_1 - \frac{\phi_1 - \phi_2}{\rho_1 - \rho_2} \cdot \rho_1 \tag{22}$$

$$\beta = \frac{\phi_1 - \phi_2}{2(\rho_1 - \rho_2)} \tag{23}$$

In addition, the deviatoric stresses for different lateral pressure combinations of the true triaxial compression can be calculated by:

$$\rho = \sqrt{2J_2} = \sqrt{\frac{1}{3}\left[(\sigma_1 - \sigma_2)^2 + (\sigma_2 - \sigma_3)^2 + (\sigma_1 - \sigma_3)^2\right]} \tag{24}$$

and the plastic inclination ϕ_1, ϕ_2 were computed according to (Papanikolaou and Kappos, 2007)：

$$\phi = \frac{\rho'}{\xi'} = \frac{\sqrt{\frac{1}{3} \cdot \left[\left(\varepsilon_1^{pl} - \varepsilon_2^{pl}\right)^2 + \left(\varepsilon_1^{pl} - \varepsilon_3^{pl}\right)^2 + \left(\varepsilon_2^{pl} - \varepsilon_3^{pl}\right)^2\right]}}{\frac{\varepsilon_1^{pl} + \varepsilon_2^{pl} + \varepsilon_3^{pl}}{\sqrt{3}}} \tag{25}$$

where the plastic strain in each principle stress direction can be solved according to Hooke's law, expressed by the following equations:

$$\left.\begin{aligned}\varepsilon_1^{pl} &= \varepsilon_1 - \left(\sigma_1 - \nu(\sigma_2+\sigma_3)\right)/E \\ \varepsilon_2^{pl} &= \varepsilon_2 - \left(\sigma_2 - \nu(\sigma_1+\sigma_3)\right)/E \\ \varepsilon_3^{pl} &= \varepsilon_3 - \left(\sigma_3 - \nu(\sigma_1+\sigma_2)\right)/E\end{aligned}\right\} \tag{26}$$

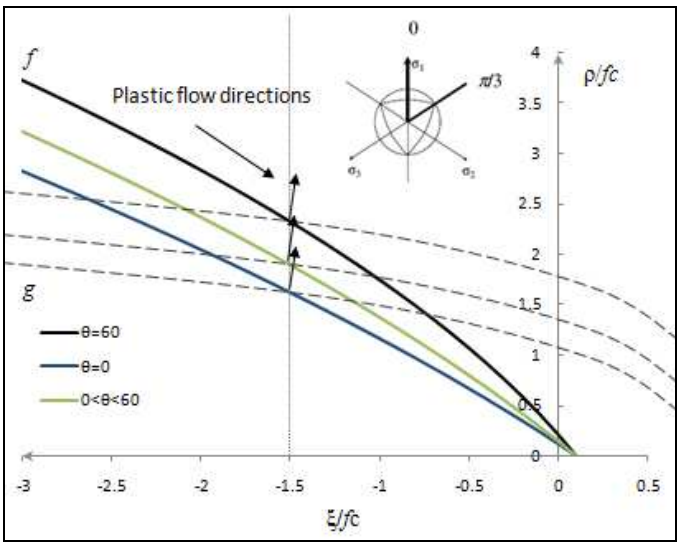

Fig.6 Consistency of plastic flow directions within the same hydrostatic stress

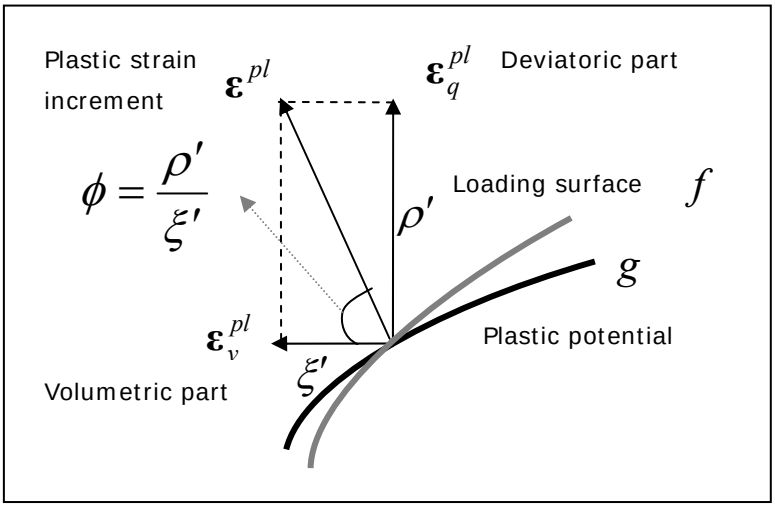

Fig.7 Inclination of plastic strain increment

By using the experimental results of peak stresses and strains, the plastic flow inclinations were thus obtained, which are listed in the Tables (3), (4) and (5). Fig.8 shows the relationship

between the plastic flow inclination and the FRI under the three lateral pressure combinations. It is interestingly found that the inclination rises with the increasing volume fraction of steel fiber (Fig.8a). Since the increase of the inclination indicates a decrease of plastic volumetric expansion rate, decaying the accumulation of plastic volumetric expansion. The steel fiber can effectively restrain the dilation. However, the polypropylene fiber has a less impact on restricting the dilation, particularly for the 3/20MPa combination (Fig.8b). The inclination tends to decrease with an increase of reinforcement index. This phenomenon is mainly attributed to that, at an early loading stage when micro crack prevails, the polypropylene fiber has certain effect on delaying the crack opening and propagation. However, once the formation of macro crack is triggered by the increasing loading, the polypropylene fiber can be easily ruptured owing to the stress concentration at the crack tip where the steel fiber plays a significant role in bridging the gap and carrying the tensile forces. It is therefore summarized that the polypropylene fiber to an extent reduces expansion during early periods thereby bridging the internal micro cracks and delaying the onset of dilation. However in the latter stage of loading, when macro cracks prevail, the contribution of polypropylene fiber on macro-crack resistance is less than steel fiber.

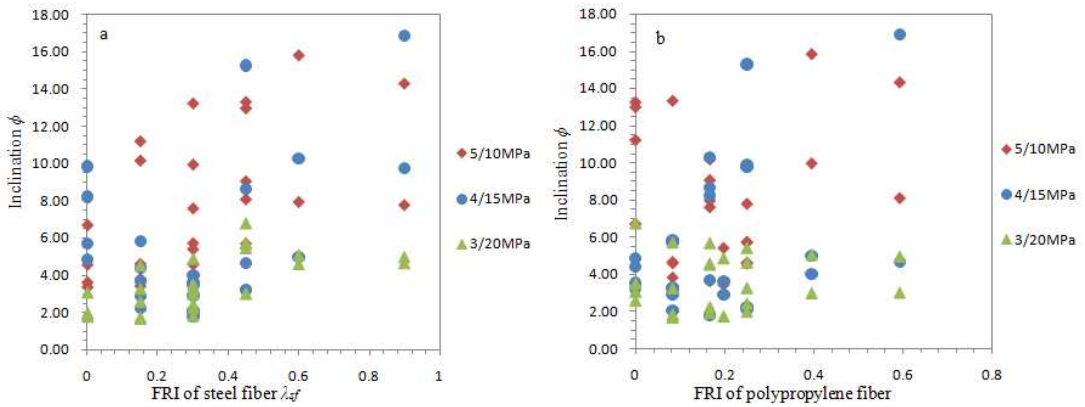

Fig.8 Relationship between the inclination and FRI: (a) steel fiber (b) polypropylene fiber

3 Constitutive equations

After ascribing the loading surface, hardening/softening law and plastic potential function, the elastoplastic formulations and the stiffness matrices were derived as following:

In the elastic range, Hooke's elastic stiffness matrix (D_{ijkl}^{el}) associates the stress strain increment with the strain increment as follows:

$$d\sigma_{ij} = D_{ijkl}^{el} d\varepsilon_{kl}^{el} = D_{ijkl}^{el}(d\varepsilon_{kl}^{tot} - d\varepsilon_{kl}^{pl}) \tag{27}$$

where the plastic strain increment vector ($d\boldsymbol{\varepsilon}^{pl}$) is evaluated via the plastic flow rule, it may be ascribed to either associate plastic potential or non-associated plastic potential, written as shown:

$$d\varepsilon_{ij}^{pl} = d\lambda \frac{\partial f}{\partial \sigma_{ij}} \tag{28}$$

wherein the plastic multiplier (λ) is determined using the consistency condition, implying that:

$$df = \frac{\partial f}{\partial \sigma_{ij}} d\sigma_{ij} + \frac{\partial f}{\partial K} \frac{\partial K}{\partial \varepsilon_{ij}^{pl}} d\varepsilon_{ij}^{pl} = 0 \tag{29}$$

where the hardening parameter *K* is a function of accumulated plastic strain in this study. $d\lambda$ is then solved as:

$$d\lambda = \frac{(\partial f / \partial \sigma_{ij}) D_{ijkl}^{el} d\varepsilon_{kl}^{tot}}{\frac{\partial f}{\partial \sigma_{mn}} D_{mnpq}^{el} \frac{\partial g}{\partial \sigma_{pq}} - \frac{\partial f}{\partial K} \frac{\partial K}{\partial \varepsilon_{ij}^{pl}} \frac{\partial g}{\partial \sigma_{ij}}} \tag{30}$$

By substituting Eq.28 and Eq.30 into Eq.27 and solving for $d\sigma_{ij}$, we obtain:

$$d\sigma_{ij} = \left(D_{ijkl}^{el} - \frac{D_{ijmn}^{el} \frac{\partial g}{\partial \sigma_{mn}} \cdot \left(\frac{\partial f}{\partial \sigma_{pq}} \right)^T D_{pqkl}^{el}}{\left(\frac{\partial f}{\partial \sigma_{rs}} \right)^T \cdot D_{rstu}^{el} \frac{\partial g}{\partial \sigma_{tu}} - \frac{\partial f}{\partial K} \frac{\partial K}{\partial \varepsilon_{ij}^{pl}} \frac{\partial g}{\partial \sigma_{ij}}} \right) d\varepsilon_{kl}^{tot} \tag{31}$$

for which the elastic stiffness matrix D_{ijkl}^{el} can be expressed as:

$$D_{ijkl}^{el} = 2G(\delta_{ik}\delta_{jl} + \frac{v}{1-2v}\delta_{ij}\delta_{kl}) \tag{32}$$

In addition, the derivatives for the loading surface function (df) are given in appendix I.

4 Integration methods

The numerical implementation of the constitutive model is specifically carried out by using a User-defined Material (UMAT) subroutine through ABAQUS, and is performed by using the explicit substepping integration algorithm with error controls. This iteration algorithm which was originally proposed by Sloan (1987) is further developed by the author for the numerical integration of elasto-plastic stress-strain rate equations of HFRC. The Newton-Raphson iteration algorithm is used to solve the non-linear finite element equations in the ABAQUS main program. Given an increment passed down from the ABAQUS main program, the intersection of initial yielding is firstly determined, and then the constitutive equations are integrated by modified Euler Scheme with user defined error tolerance. According to this scheme, the constitutive equations are first integrated by using Euler scheme which is of first order accuracy, followed by using the modified Euler scheme which is of second order accuracy. The integration error is determined by the difference between the integration results of these two schemes. If the integration error is smaller than the prescribed error tolerance, the size of the next subincrement is determined by extrapolation according to the current error compared with the error tolerance. If the integration error is larger than the error tolerance, the size of the current subincrement is reduced based on the ratio of the current error with the error tolerance. Thus, this scheme can automatically divide the imposed strain increment according to the prescribed integration error tolerance. Subsequently, a correction of stress-state is applied according to Abbo (1997). Finally, the elasto-plastic stiffness matrix is updated and sent back to ABAQUS to obtain the stress-strain relation for current increment.

The algorithm for each integration point for a given strain rate $\Delta\varepsilon_{kl}^{tot}$ in a finite time step $\Delta t = \Delta t_{k+1} - t_k$ is briefly summarized in the following steps:

1) Evaluate yield condition

$$\Delta\sigma_{ij}^{e} = D_{ijkl}^{el}\Delta\varepsilon_{kl}^{tot} \tag{33}$$

If $f(\sigma_{ij}^{k}, K_0) < 0$ and $f(\sigma_{ij}^{k} + \Delta\sigma_{ij}^{e}, K_0) > 0$ go to 2)

Else $\sigma_{ij}^{k+1} = \sigma_{ij}^{k} + \Delta\sigma_{ij}^{e}$ (34)

$$D_{ijkl}^{ep} = D_{ijkl}^{el} \tag{35}$$

2) Intersection scheme that find a factor β to determine the onset of initial yield as:

$$f(\sigma_{ij}^{k} + \beta\cdot\Delta\sigma_{ij}^{e}, K_0) = 0 \tag{36}$$

and factor β is set to 0 if the increment causes purely plastic deformation. It is noted that the yield condition control from Eq.36 can be approximated as (see Fig.9):

$$\left| f(\sigma_{ij}^{k} + \beta\cdot\Delta\sigma_{ij}^{e}, K_0) \right| \le TOL \tag{37}$$

Applying the above Eq.37 can lead to an efficient convergence of the calculation with relative effective precision. Here, *TOL* indicates a small positive tolerance with a recommended interval of ranging from 10^{-9} to 10^{-6}.

(2.1) Set $f_0 = f(\sigma_{ij}^{k} + \beta_0\cdot\Delta\sigma_{ij}^{e}, K_0)$ and $f_1 = f(\sigma_{ij}^{k} + \beta_1\cdot\Delta\sigma_{ij}^{e}, K_0)$. Initial values for β_0, β_1 can be assigned as $\beta_0 = 0$ and $\beta_1 = 1$.

(2.2) Calculate β by using Newton-Raphson iterative scheme:

$$\beta = \beta_1 - \frac{f_1}{f_1 - f_0}(\beta_1 - \beta_0) \quad (\beta_0 = 0 \text{ and } \beta_1 = 1) \tag{38}$$

(2.3) Set $f_{new} = f(\sigma_{ij}^{k} + \beta\cdot\Delta\sigma_{ij}^{e}, K_0)$ and specify tolerance *TOL*.

If $|f_{new}| \le TOL$ then go to step 3).

else If $f_{new}\cdot f_0 < 0$ then $\beta_1 = \beta$

else If $f_{new} \cdot f_0 > 0$ then $\beta_0 = \beta$

Repeat step (2.1)-(2.3).

3) Modified Euler integration algorithm with error control

(3.1)Initialize parameter $T = 0$ and $\Delta T = 1$ for current increment, if T<1, then cycle step (3.2)-(3.6).

(3.2)Calculate the first estimate of stress increment $\Delta\boldsymbol{\sigma}_1$ using Euler scheme:

$$\Delta\boldsymbol{\sigma}_1 = (1-\beta)\Delta\sigma_{ij}^e \cdot \Delta T - \Delta\lambda_1 D_{ijkl}^{el} \frac{\partial g}{\partial \boldsymbol{\sigma}_1} \tag{39}$$

and the first hardening increment ΔK_1 according to Eq.7:

$$\Delta K_1 = H_p(k,s) \cdot \Delta\lambda_1 \frac{\partial g}{\partial \boldsymbol{\sigma}_1} \tag{40}$$

Where $$\Delta\lambda_1 = \max\left\{ \frac{\left(\frac{\partial f}{\partial \boldsymbol{\sigma}_1}\right)^T \cdot (1-\beta)\Delta\sigma_{ij}^e \cdot \Delta T}{\left(\frac{\partial f}{\partial \boldsymbol{\sigma}_1}\right)^T D_{ijkl}^{el} \frac{\partial g}{\partial \boldsymbol{\sigma}_1} - \frac{\partial f}{\partial K} \cdot H_p(k,s) \cdot \frac{\partial g}{\partial \boldsymbol{\sigma}_1}}, 0 \right\}$$

(3.3)Calculate the second estimate of stress increment $\Delta\boldsymbol{\sigma}_2$ using modified Euler scheme:

$$\Delta\boldsymbol{\sigma}_2 = (1-\beta)\Delta\sigma_{ij}^e \cdot \Delta T - \Delta\lambda_2 D_{ijkl}^{el} \frac{\partial g}{\partial \boldsymbol{\sigma}_2} \tag{41}$$

and the second hardening increment ΔK_2:

$$\Delta K_2 = H_p(k,s) \cdot \Delta\lambda_2 \frac{\partial g}{\partial \boldsymbol{\sigma}_2} \tag{42}$$

where $$\Delta\lambda_2 = \max\left\{ \frac{\left(\frac{\partial f}{\partial \boldsymbol{\sigma}_2}\right)^T \cdot (1-\beta)\Delta\sigma_{ij}^e \cdot \Delta T}{\left(\frac{\partial f}{\partial \boldsymbol{\sigma}_2}\right)^T D_{ijkl}^{el} \frac{\partial g}{\partial \boldsymbol{\sigma}_2} - \frac{\partial f}{\partial K'} \cdot H_p(k,s) \cdot \frac{\partial g}{\partial \boldsymbol{\sigma}_2}}, 0 \right\}$$

$$\boldsymbol{\sigma}_2 = \boldsymbol{\sigma}_1 + \Delta\boldsymbol{\sigma}_1, \quad K' = K + \Delta K_1 \tag{43}$$

(3.4)Update the more accurate estimate stress increment as well as hardening parameter increment as:

$$\Delta\hat{\boldsymbol{\sigma}} = \frac{\Delta\boldsymbol{\sigma}_1 + \Delta\boldsymbol{\sigma}_2}{2}, \quad \Delta\hat{K} = \frac{\Delta K_1 + \Delta K_2}{2} \tag{44}$$

(3.5)Determine the local truncation error for the substep from

$$Error = \max\left\{\frac{\left\|\Delta\sigma_2 - \Delta\sigma_1\right\|}{2\left\|\Delta\hat{\sigma}\right\|}, \frac{\left|\Delta K_2 - \Delta K_1\right|}{2\left|\Delta\hat{K}\right|}\right\} \tag{45}$$

If the *Error*<*TOL*, then

$$\hat{K} = K + \Delta\hat{K} \tag{46}$$

$$\hat{\boldsymbol{\sigma}} = \boldsymbol{\sigma}_1 + \Delta\hat{\boldsymbol{\sigma}} \tag{47}$$

$$T = T + \Delta T \tag{48}$$

and the ΔT for the next substep is extrapolated as:

$$\Delta T = q\Delta T \tag{49}$$

$$q = \min\left\{0.9(TOL/Error)^{1/2}, 1.1\right\} \tag{50}$$

If the *Error*>*TOL*, this substep fails, a smaller time step is decreased, and the above computations are carried out again by using a reduced subincrement as:

$$\Delta T = q'\Delta T \tag{51}$$

An estimate value for q' can be defined as:

$$q' = \max\left\{0.8(TOL/Error)^{1/2}, 0.1\right\} \tag{52}$$

(3.6)The sub increment is finished and exits with the updated accumulated stresses as:

$$\boldsymbol{\sigma}^{T+\Delta T} = \hat{\boldsymbol{\sigma}} \quad , \quad K^{T+\Delta T} = \hat{K} \tag{53}$$

4) Correction of stress state (Abbo,1997)

$$\boldsymbol{\sigma}_{correct} = \boldsymbol{\sigma}^{T+\Delta T} - \Psi \cdot D^{el}_{ijkl} \cdot \frac{\partial g}{\partial \boldsymbol{\sigma}^{T+\Delta T}} \tag{54}$$

$$\Psi = \frac{f(\boldsymbol{\sigma}^{T+\Delta T}, K_{correct})}{\left(\frac{\partial f}{\partial \boldsymbol{\sigma}^{T+\Delta T}}\right)^T D^{el}_{ijkl} \frac{\partial g}{\partial \boldsymbol{\sigma}^{T+\Delta T}} - \frac{\partial f}{\partial K_{correct}} \cdot H_p(k,s) \cdot \frac{\partial g}{\partial \boldsymbol{\sigma}^{T+\Delta T}}} \tag{55}$$

$$K_{correct} = H_p(k,s) \cdot \Psi \cdot \frac{\partial g}{\partial \boldsymbol{\sigma}^{T+\Delta T}} \tag{56}$$

If $|f(\boldsymbol{\sigma}_{correct}, K_{correct})| \leq |f(\boldsymbol{\sigma}^{T+\Delta T}, K^{T+\Delta T})|$ then

$$\sigma^{k+1}_{ij} = \boldsymbol{\sigma} = \boldsymbol{\sigma}_{correct}, \quad K^{k+1} = K_{correct} \tag{57}$$

$$\text{else} \quad \sigma^{k+1}_{ij} = \boldsymbol{\sigma} = \boldsymbol{\sigma}^{T+\Delta T}, K^{k+1} = K^{T+\Delta T} \tag{58}$$

5) Update the elasto-plastic stiffness matrix as:

$$\boldsymbol{D}^{ep} = \left\{ \boldsymbol{D}^{el} - \frac{\boldsymbol{D}^{el} \frac{\partial g}{\partial \boldsymbol{\sigma}} \cdot \left(\frac{\partial f}{\partial \boldsymbol{\sigma}}\right)^T \boldsymbol{D}^{el}}{\left(\frac{\partial f}{\partial \boldsymbol{\sigma}}\right)^T \boldsymbol{D}^{el} \frac{\partial g}{\partial \boldsymbol{\sigma}} - \frac{\partial f}{\partial K^{k+1}} \cdot H_p(k,s) \cdot \frac{\partial g}{\partial \boldsymbol{\sigma}}} \right\} \tag{59}$$

This stiffness matrix determined by the integration subroutine is then given to the ABAQUS main program to obtain the stress-strain relation for the current increment.

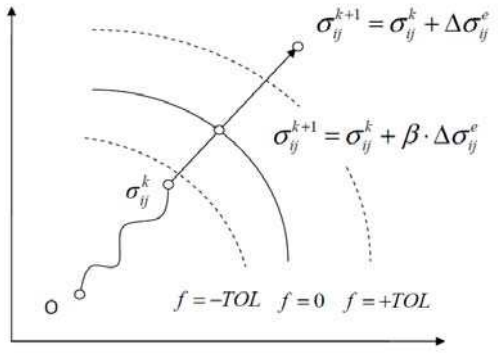

Fig.9 Determination of yield surface intersection

5 Validations

In the first place, the coefficients α, β which control the direction of plastic flow were calibrated in accordance to the approach described in previous section 2.4 and determined using the test results from lateral pressure combinations of 5/10MPa and 3/20MPa. The

responses of the constitutive model were then compared to the results of 4/15MPa to check its validity. Figs.10 to 13 compare the analytical and experimental volumetric-axial strain behaviors of HFRC under a 4/15MPa lateral pressure combination, wherein both associate and non-associate flow rule were applied to show the difference in volumetric dilation. For non-associated flow rule, the calibration factors of plastic potential function were determined as $\alpha = -2.86, \beta = 0.038$ for SA05PA05 , $\alpha = -16.1, \beta = 0.135$ for SA10PA10, $\alpha = -12.26, \beta = 0.12$ for SA15PA10，and $\alpha = 3.84, \beta = 0.01$ for SA15PA15. As shown in the plots, HFRC exhibits significant non-associate plasticity, the constitutive model with non-associate flow provides a more precise prediction of the volumetric strain-axial strain behavior. On the other hand, the associate flow rule excessively overestimates the plastic dilatancy.

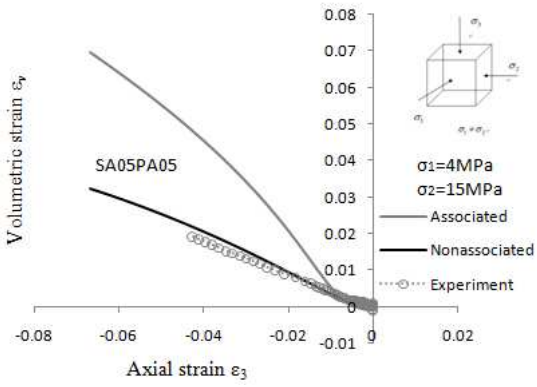

Fig.10 $\varepsilon_3 - \varepsilon_v$ curve (SA05PA05)

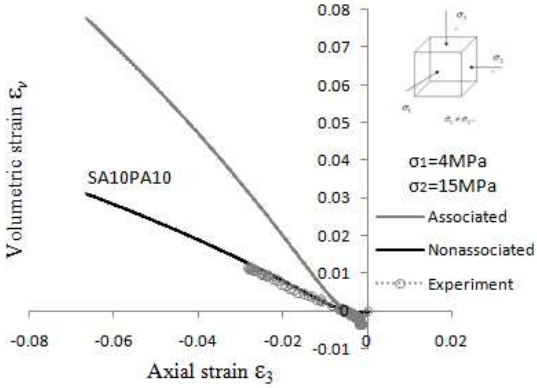

Fig.11 $\varepsilon_3 - \varepsilon_v$ curve (SA10PA10)

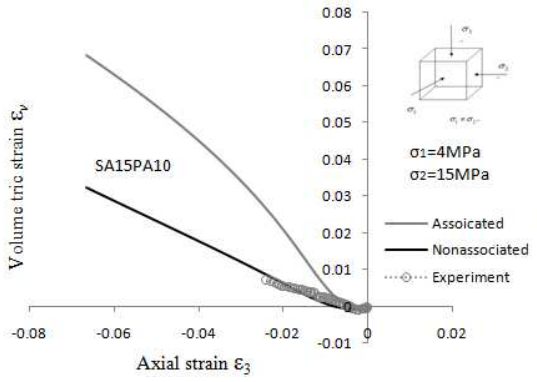

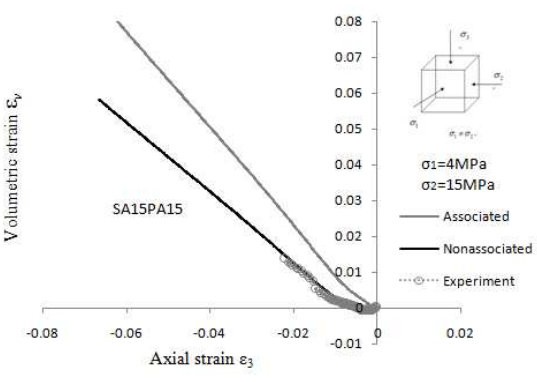

Fig.12 $\varepsilon_3 - \varepsilon_v$ curve (SA15PA10) Fig.13 $\varepsilon_3 - \varepsilon_v$ curve (SA15PA15)

Fig.14 shows the corresponding directions of plastic strain vectors for SA05PA05, SA10PA10, SA15PA10 and SA15PA15 at failure surface. It is observed that the direction of plastic flow invariably approaches the deviatoric stress axis when various hybrid fiber volume fractions are introduced, resulting in a decrease of volumetric growth rate (dilation rate). The plastic strain direction approaching the deviatoric stress axis causes a slower accumulation of the volumetric plastic strain component, thereby delaying ultimate failure consequently improving capacity in both axial and lateral directions.

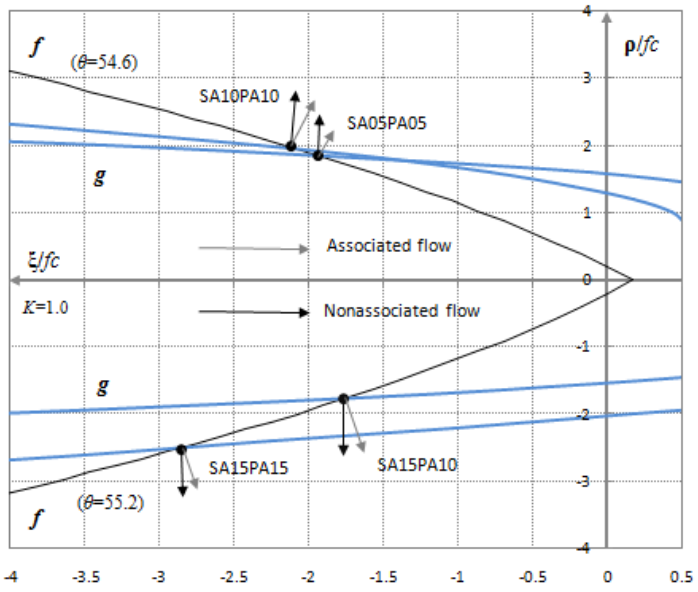

Fig.14 Plastic flow direction of HFRC at failure surface

6 Verifications

The constitutive relations were specifically incorporated into the proposed constitutive model via the UMAT subroutine by running an ABAQUS command "ABAQUS JOB=*name*.INP USER=*name* INT". Apart from the proposed constitutive model, the development of an appropriate and separate finite element model was undertaken in this study. In view of the loading

situation in true triaxial compression with no bending moment and bending deformation of the specimen observed, a 'C3D8' element, which is an iso-parametric, eight-noded solid element, was selected for the numerical simulation, with the finite element mesh and boundary conditions as shown in Fig.15.

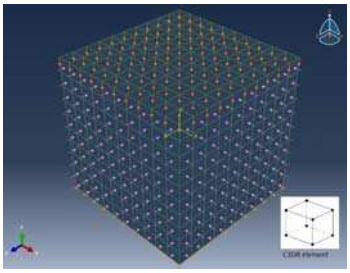

Fig.15 Finite element mesh with C3D8 elements

During the multiaxial compression simulation, displacement loading control is used and an initial value of hardening function K_0=0.4 is applied to determine the elastic range. All the relevant model input parameters under consideration (i.e. $k_c, k_t, a, b, \varepsilon_c$ values and plastic potential parameters α, β values) were firstly calibrated to enable comparisons between the selected experimental investigations using the developed equations in the previous section.

To verify the developed constitutive model and the aforementioned integration scheme, the stress-strain response is evaluated for both conventional concrete and fiber reinforced concrete.

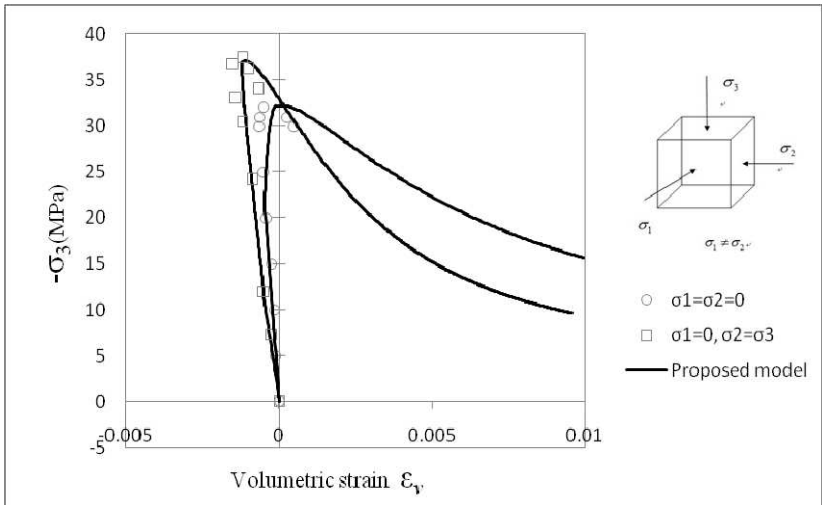

Fig.16 Principal stress-volumetric strain behavior of samples subjected to both uniaxial and biaxial compression as reported by Kupfer et al., (1969)

Fig.16 compares the analytical results of principal stress-volumetric strain relations to the experimental results of Kupfer et al., (1969) for plain concrete under both uniaxial and equibiaxial compressions. For $f_{cu}=32.1$MPa, $E=2.9\times e^4$MPa, as in Kupfer et al., (1969), apart from the values of k_c, and k_t, which are kept constant (k_c=k_t=1) calculated using Eqs.(5) and (6), the other model parameters were respectively calibrated to $a=1.727$, $b=0.109$ and $\varepsilon_c=0.00149$ for uniaxial compression, $\varepsilon_c=0.00172$ for equibiaxial compression, and the plastic potential parameter were set to $\alpha=7.75, \beta=-0.064$ which were calibrated by the peak stresses and strains of two boundary conditions, i.e. the peak stresses and strains in uniaxial compression and biaxial compression. The comparison shown in the plots proves that the proposed model has the capability to accurately describe the stress-strain behavior as well as the volumetric deformation of plain concrete.

In addition, the results of laterally confined triaxial compression tests conducted on plain concrete were compared to the model's prediction. The experimental curves derived by Candappa et al., (2000) for high strength concrete subjected to relative low lateral confining pressures were compared with the analytical results, as illustrated in Fig.17, where $f_{cu}=60.6$ MPa, $E=3.8\times e^4$MPa, and confining pressures of 0MPa, 4MPa, 8MPa were individually considered. The model parameters were calibrated to $a=1.089, b=0.129$, and $\varepsilon_c=0.00205$ for uniaxial compression(σ_1=σ_2=0), $\varepsilon_c=0.00746$ and $\varepsilon_c=0.01287$ for laterally confined triaxial compression (σ_1=σ_2=-4MPa) and (σ_1=σ_2=-8MPa) respectively. In addition, the plastic potential coefficients were calibrated by means of peak stresses and strains in uniaxial compression and multiaxial compression with a lateral confinement of σ_1=σ_2=-4MPa, which were determined to

$\alpha = 11.25, \beta = -0.092.$

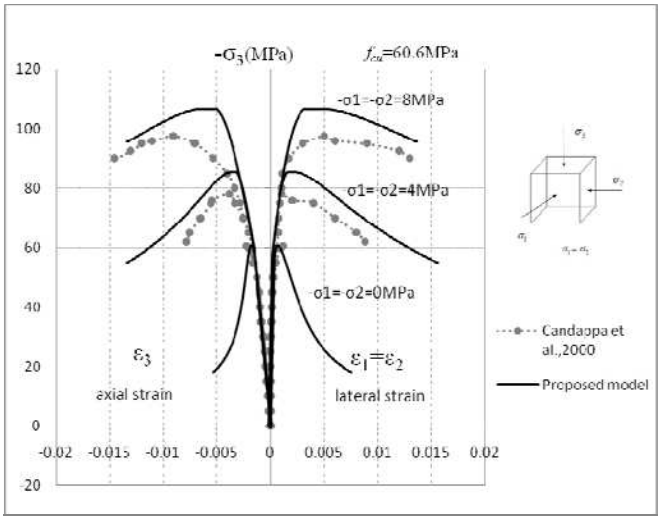

Fig.17 Comparison of stress-strain curves of experimental results for high strength concrete as reported by Candappa et al., (2000) and the constitutive model's prediction under low confining pressures

It is clear that although the proposed model slightly overestimates the triaxial strength (i.e. within +10% of the experimental values), it still reflects the concrete's expected behavior, in that the strength and ductility are significantly improved owing to the lateral confinement.

Furthermore, for HFRC materials, Fig.18 shows the comparison between the predicted curves and experimental results of HFRC (with steel fiber volume fraction ranging from 0.5% to 1.5% and aspect ratio of 30, and polypropylene fiber at 0.1% fixed volume fraction and aspect ratio of 167) under uniaxial compression as reported by Zhang (2010). Based on Zhang's test with $f_{cu} = 28.6$ MPa and $E = 2.9 \times e^4$ MPa, the model parameters were calibrated as shown below: a=1.83, b=0.064, k_c=1.0084, k_t=1.034, $\varepsilon_c = 0.00147$ (for SA05PA10), a=1.902, b=0.06, k_c=1.0168, $\varepsilon_c = 0.00149$ (for SA10PA10), a=1.974, b=0.056, k_c=1.0252, k_t=1.058 $\varepsilon_c = 0.00151$ (for SA15PA10). The plastic potential coefficients were input according to the value calibrated from present true triaxial compression results as: $\alpha = -16.94, \beta = 0.165$ for (for SA05PA10), $\alpha = -16.1, \beta = 0.135$ (for SA10PA10) $\alpha = -12.26, \beta = 0.12$ for (for SA15PA10).

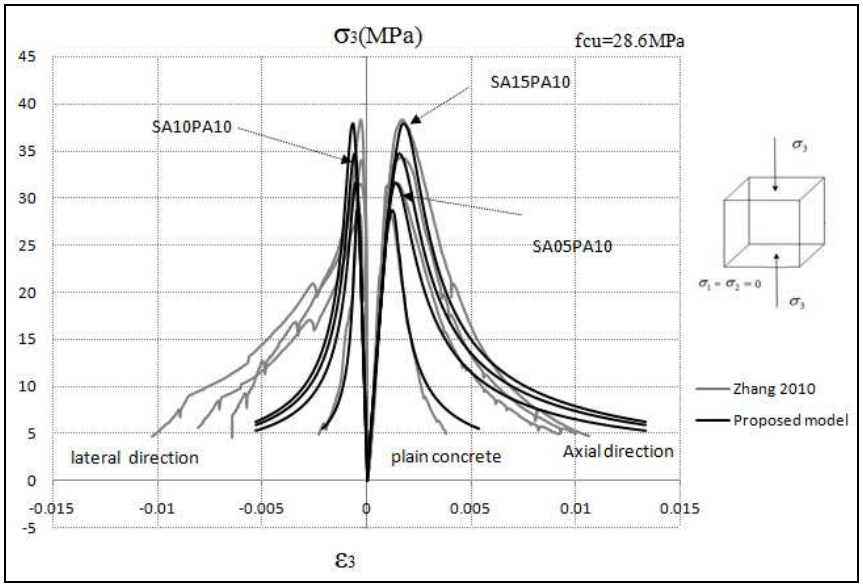

Fig.18 Comparison of HFRC uniaxial stress-strain relationships of constitutive model analytical results and experimental results reported by Zhang (2010)

As illustrated in Fig.18, very good conformance exists between the experimental and analytical curves of HFRC where both strength and axial deformation are concerned, with the exception of a moderate underestimation of the strain in lateral direction. From the comparisons shown above, it is found that the proposed constitutive model gives good prediction of the evaluated experimental stress-strain curves for HFRC materials. It is believed, having conducted relevant comparisons that the proposed model can be applied to other subsequent numerical simulations of fiber reinforced concrete.

6 Conclusions

A plasticity-based constitutive model for HFRC was developed, which comprises a five-parameter failure criterion in addition to uncoupled isotropic hardening and softening regimes determined by accumulated equivalent plastic strain and a nonlinear non-associated plastic potential. The fiber reinforcement indices of HFRC are introduced into the constitutive model to take the fiber effect into account.

The proposed constitutive model was implemented into the FE package ABAQUS through the UMAT subroutine based on an explicit integration algorithm. The subroutine utilizes a Modified Newton-Raphson technique to determine the initial yield point, a modified Euler integration algorithm with error control to calculate the unknown stress state after yielding, and a substepping scheme for stress state correction. The algorithm is applicable to the numerical simulation of fiber reinforced concrete materials by simply incorporating the corresponding yield criterion, hardening law and plastic potential function.

The responses of the developed model were verified using multiaxial compression experimental results for both plain and fiber reinforced concrete. It has been shown that the proposed constitutive model agrees with the evaluated experimental stress-strain curves in reasonable accuracy.

With respect to HFRC material, it exhibits significant non-associate plasticity. The constitutive model with non-associate flow provides a more precise prediction of the volumetric strain-axial strain behavior. It is observed that the direction of plastic flow invariably approaches the deviatoric stress axis when various hybrid fiber volume fractions are introduced, resulting in a decrease of dilation rate.

Acknowledgement

The author is grateful to the support granted by CSC funding. This study reported is a part of the NSFC project (No. 51078295).

Reference

Abbo, A.J. 1997. Finite element algorithms for elastoplasticity and consolidation, Ph.D Thesis, University of Newcastle, Australia.

ACI Committee 544, 1982. State-of-the-art report on fiber reinforced concrete. American Concrete

Institute, Detroi.

Babu, R.R., Gurmail, S.B., Arbind, K.S., 2005. Constitutive modeling of concrete: An overview, Asian Journal of Civil Engineering 6, 211-246.

Bayasi, Z., Zeng, J., 1993. Properties of polypropylene fiber reinforced concrete, ACI Material Journal 90, 605-610.

Bentur, A., Mindess, S., 1990. Fiber Reinforced Cementitious Composites. Elsevier Applied Science, London.

Candappa, D.C., Sanjayan, J.G., Setunge, S., 2001. Complete triaxial stress-strain curves of high-strength concrete, Journal of Materials in Civil Engineering 13, 209–215.

Chern, J.C., Yang, H.J., Chen, H.W., 1992. Behavior of steel fiber reinforced concrete in multiaxial loading. ACI Material Journal 89, 32-40.

Chi, Y., 2012. Plasticity Theory Based Constitutive Modelling of Hybrid Fibre Reinforced Concrete, Ph.D Thesis, the University of Nottingham, UK.

Chi, Y., Xu L.H.,Yu, H.S., 2013. Plasticity Model for Hybrid Fiber Reinforced Concrete under True Triaxial Compression, Journal of Engineering Mechanics, 10.1061/(ASCE)EM.1943-7889.0000659.

Guo, Z.H., 1997. The strength and deformation of concrete—experimental results and constitutive relationship, Tsinghua University Press, Beijing.

Grassl, P., Lundgren, K., Gylltoft, K., 2002. Concrete in compression: a plasticity theory with a novel hardening law. International Journal of Solids and Structures 39, 5205–5223.

Hu, X.D., Day, R., Dux, P., 2003. Biaxial failure model for fiber reinforced concrete. Journal of Materials in Civil Engineering 15, 609-615.

Imran, I., Pantazopoulou, S.J., 2001. Plasticity model for concrete under triaxial compression. Journal of Engineering Mechanics 3, 281-290.

Kupfer, H., Hilsdorf, H. K., Rusch, H., 1969. Behavior of Concrete under Biaxial Stresses. ACI Journal Proceedings 66(8), 656-666.

Lu, X., Hsu, C.T.T., 2006. Behavior of high strength concrete with and without steel fiber reinforcement in triaxial compression. Cement and Concrete Research 36, 1679–1685.

Murugappan, K., Paramasivam, P., Tan, K.H., 1993.Failure envelope for steel fiber concrete under biaxial compression, Journal of Materials in Civil Engineering 5, 436-446.

Papanikolaou, V.K., Kappos, A.J., 2007. Confinement-sensitive plasticity constitutive model for concrete in triaxial compression. International Journal of Solids and Structures 44, 7021-7048.

Park, H., Kim, J.Y., 2005. Plasticity model using multiple failure criteria for concrete in compression. International Journal of Solids and Structures 42, 2303–2322.

Qian, C.X., Stroeven, P., 2000. Development of hybrid polypropylene-steel fibre-reinforced concrete. Cement and Concrete Research 30, 63-69.

Seow, P.E.C., Swaddiwudhipong, S., 2005. Modelling of steel fiber-reinforced concrete under multi-axial loads. Cement and Concrete Research 36, 1354-1361.

Sloan, S.W., 1987. Substepping schemes for the numerical integration of elastoplastic stress-strain relations, International Journal of Numerical Methods in Engineering 24, 893-911.

Song, Y.P., Zhao, G.F., Peng, F., 1996. Strength behavior and failure criterion of steel fiber concrete under triaxial stresses. Journal of Civil Engineering 29, 14-23.

Swamy, R.N., Barr, B., 1989. Fiber reinforced cements and concretes: recent developments. Elservier Science Publisher LTD, New York.

Tavakoli, M., 1994. Tensile and compressive strengths of polypropylene fiber reinforced concrete.

SP142-04, 142, 61-72.

Willam, K. J., Warnke, E. P., 1974. Constitutive model for the triaxial behavior of concrete (paper III-l), Seminar on Concr. Struct. Subjected to Triaxial Stresses, Int. Assoc, of Bridge and Struct. Engrg.. 19, 1-30.

Xu, L.H., Xia, D.T , Xia, G.Z., Chi, Y., 2007. Effect of steel fiber and polypropylene fiber on the strength of high strength concrete. Journal of Wuhan University of Technology 29, 58-60.

Yu, H.S., 2006. Plasticity and Geotechnics, Springer.

Zhang, Y., 2010. Study on Uniaxial Compressive Constitutive Relationship and Uniaxial Tensile Behavior of Steel-Polypropylene Hybrid Fiber Reinforced Concrete, Ph.D Thesis, Wuhan University, China.

Appendix I: Derivatives of the loading surface function

For a convenient description of the derivatives of loading surface function, the failure surface (Eq.4) is alternatively expressed as:

$$\rho^{hf}\left(\xi,\theta\right)=\frac{s+vw}{u} \tag{I1}$$

$$\text{where}\begin{cases} s=2\rho_c^{hf}[(\rho_c^{hf})^2-(\rho_t^{hf})^2\cos\theta] \\ v=\rho_c^{hf}(2\rho_t^{hf}-\rho_c^{hf}) \\ w=\{4[(\rho_c^{hf})^2-(\rho_t^{hf})^2]\cos^2\theta+5(\rho_t^{hf})^2-4\rho_t^{hf}\rho_c^{hf}\}^{1/2} \\ u=4[(\rho_c^{hf})^2-(\rho_t^{hf})^2]\cos^2\theta+(\rho_c^{hf}-2\rho_t^{hf})^2 \end{cases} \tag{I2}$$

The gradient of $\dfrac{\partial f}{\partial\sigma_{ij}}$ is given by:

$$\frac{\partial f}{\partial\sigma_{ij}}=\frac{\partial f}{\partial I_1}\cdot\frac{\partial I_1}{\partial\sigma_{ij}}+\frac{\partial f}{\partial J_2}\cdot\frac{\partial J_2}{\partial\sigma_{ij}} \tag{I3}$$

In which

$$\frac{\partial I_1}{\partial\sigma_{ij}}=\delta_{ij}\,,\ \frac{\partial J_2}{\partial\sigma_{ij}}=S_{ij} \tag{I4}$$

$$\frac{\partial f}{\partial I_1}=-K\left(\bar{\varepsilon}_p\right)\cdot\frac{\partial\rho^{hf}\left(\xi,\theta\right)}{\partial I_1}=-K\left(\bar{\varepsilon}_p\right)\cdot\left(\frac{\partial\rho^{hf}\left(\xi,\theta\right)}{\partial\rho_c^{hf}}\cdot\frac{\partial\rho_c^{hf}}{\partial I_1}+\frac{\partial\rho^{hf}\left(\xi,\theta\right)}{\partial\rho_t^{hf}}\cdot\frac{\partial\rho_t^{hf}}{\partial I_1}\right) \tag{I5}$$

$$\text{where}\begin{cases}\dfrac{\rho_c^{hf}}{f_{cu}}=-\dfrac{1}{2b_2}\left[b_1+\sqrt{b_1^2-4b_2\left(b_0-\dfrac{\xi}{f_{cu}}\right)}\right]\cdot k_c\\ \dfrac{\rho_t^{hf}}{f_{cu}}=-\dfrac{1}{2a_2}\left[a_1+\sqrt{a_1^2-4a_2\left(a_0-\dfrac{\xi}{f_{cu}}\right)}\right]\cdot k_t\\ \dfrac{\partial\rho_c^{hf}}{\partial I_1}=\dfrac{\partial\rho_c^{hf}}{\partial\xi}\cdot\dfrac{\partial\xi}{\partial I_1}=-k_c\cdot\dfrac{1}{\sqrt{b_1^2-4b_2\left(b_0-\dfrac{\xi}{f_{cu}}\right)}}\cdot\dfrac{1}{\sqrt{3}}\\ \dfrac{\partial\rho_t^{hf}}{\partial I_1}=\dfrac{\partial\rho_t^{hf}}{\partial\xi}\cdot\dfrac{\partial\xi}{\partial I_1}=-k_t\cdot\dfrac{1}{\sqrt{a_1^2-4a_2\left(a_0-\dfrac{\xi}{f_{cu}}\right)}}\cdot\dfrac{1}{\sqrt{3}}\end{cases}\tag{I6}$$

and

$$\frac{\partial\rho^{hf}(\xi,\theta)}{\partial\rho_c^{hf}}=\frac{u\left(\dfrac{\partial s}{\partial\rho_c^{hf}}+\dfrac{\partial v}{\partial\rho_c^{hf}}\cdot w+v\cdot\dfrac{\partial w}{\partial\rho_c^{hf}}\right)-(s+vw)\cdot\dfrac{\partial u}{\partial\rho_c^{hf}}}{u^2}\tag{I7}$$

$$\begin{cases}\dfrac{\partial s}{\partial\rho_c^{hf}}=6\left(\rho_c^{hf}\right)^2\cdot\cos\theta-2\left(\rho_t^{hf}\right)^2\cdot\cos\theta\\ \dfrac{\partial v}{\partial\rho_c^{hf}}=2\rho_t^{hf}-2\rho_c^{hf}\\ \dfrac{\partial w}{\partial\rho_c^{hf}}=\dfrac{8\cos^2\theta\cdot\rho_c^{hf}-4\rho_t^{hf}}{2w}\\ \dfrac{\partial u}{\partial\rho_c^{hf}}=8\cos^2\theta\cdot\rho_c^{hf}+2\left(\rho_c^{hf}-2\rho_t^{hf}\right)\end{cases}\tag{I8}$$

$$\frac{\partial\rho^{hf}(\xi,\theta)}{\partial\rho_t^{hf}}=\frac{u\left(\dfrac{\partial s}{\partial\rho_t^{hf}}+\dfrac{\partial v}{\partial\rho_t^{hf}}\cdot w+v\cdot\dfrac{\partial w}{\partial\rho_t^{hf}}\right)-(s+vw)\cdot\dfrac{\partial u}{\partial\rho_t^{hf}}}{u^2}\tag{I9}$$

$$\begin{cases}\dfrac{\partial s}{\partial\rho_c^{hf}}=-2\rho_c^{hf}\cdot\cos\theta\cdot2\rho_t^{hf}\\ \dfrac{\partial v}{\partial\rho_c^{hf}}=2\rho_c^{hf}\\ \dfrac{\partial w}{\partial\rho_c^{hf}}=\dfrac{-8\cos^2\theta\cdot\rho_t^{hf}+10\rho_t^{hf}-4\rho_c^{hf}}{2w}\\ \dfrac{\partial u}{\partial\rho_c^{hf}}=-8\cos^2\theta\cdot\rho_t^{hf}-4\left(\rho_c^{hf}-2\rho_t^{hf}\right)\end{cases}\tag{I10}$$

Besides,

$$\frac{\partial f}{\partial J_2} = \frac{\sqrt{2}}{2} \cdot \frac{1}{\sqrt{J_2}} - K(\bar{\varepsilon}_p) \cdot \frac{\partial \rho^{hf}(\xi,\theta)}{\partial \cos\theta} \cdot \frac{\partial \cos\theta}{\partial J_2} \tag{I11}$$

where

$$\frac{\partial \cos\theta}{\partial J_2} = \left(\frac{2\sigma_3 - \sigma_2 - \sigma_1}{2\sqrt{3}} \right) \cdot \left(-\frac{1}{2} \right) \cdot J_2^{-3/2} \quad \text{for} \quad \sigma_3 \geq \sigma_2 \geq \sigma_1 \tag{I12}$$

and

$$\frac{\partial \rho^{hf}(\xi,\theta)}{\partial \cos\theta} = \frac{u\left(\frac{\partial s}{\partial \cos\theta} + \frac{\partial v}{\partial \cos\theta} \cdot w + v \cdot \frac{\partial w}{\partial \cos\theta} \right) - (s + vw) \cdot \frac{\partial u}{\partial \cos\theta}}{u^2} \tag{I13}$$

$$\begin{cases} \dfrac{\partial s}{\partial \cos\theta} = 2\rho_c^{hf} \cdot \left[\left(\rho_c^{hf}\right)^2 - \left(\rho_t^{hf}\right)^2 \right] \\ \dfrac{\partial v}{\partial \cos\theta} = 0 \\ \dfrac{\partial w}{\partial \cos\theta} = \dfrac{4\cos\theta \cdot \left[\left(\rho_c^{hf}\right)^2 - \left(\rho_t^{hf}\right)^2 \right]}{w} \\ \dfrac{\partial u}{\partial \cos\theta} = 8\left[\left(\rho_c^{hf}\right)^2 - \left(\rho_t^{hf}\right)^2 \right] \cdot \cos\theta \end{cases} \tag{I14}$$